JOURNAL OF MATERIALS SCIENCE 26 (1991) 3107–3118

Weibull strength statistics for graphite fibres measured from the break progression in a model graphite/glass/epoxy microcomposite

R. GULINO*, S. L. PHOENIX
Sibley School of Mechanical and Aerospace Engineering, Upson Hall, Cornell University, Ithaca, NY 14853, USA

Recent statistical theories for the failure of fibrous composities focus on the initiation and growth of clusters of broken fibres within the composite. These theoreis require the probability distribution for fibre strength at the length scale of micromechanical load transfer around a cluster of broken fibres. Such lengths are of the order of 10 to 150 fibre diameters, and thus the associated strengths have previously been unmeasurable by direct means. Using Weilbull/weakest-link rules, researchers have resorted to extrapolation of tension test results from gauge lengths two orders of magnitude longer. In this paper, a technique is developed to study the break progression of a single graphite fibre in an epoxy microcomposite tape, where the graphite fibre is flanked by two, proof-tested, glass fibres. These results are interpreted using a Weibull/Poisson model of the break progression, the number of breaks in the graphite fibre as a function of applied strain, which accounts for stress decay at the fibre ends. It is shown that such extrapolations of tension test data are too optimistic. In addition, different fibres from the same yarn cross-section, apparently have different flaw populations, unlike that which occurs at longer gauge lengths.

1. Introduction

In a widely accepted statistical model for the failure of a unidirectional composite, the composite is viewed as a chain of short bundles under tension. Failure of the composite is caused by the failure of the weakest bundle, whose failure is initiated by the failure of single fibres within the bundle. Various versions of the model have been studied both in the setting of short-term strength [1–8] and long-term, creep-rupture [9, 10]. Within a bundle, the fibres share load according to a rule which reflects lateral load transfer from failed to surviving fibres through shear in the matrix. The length of a bundle is characteristically an effective load transfer length for a fibre adjacent to a break, an idea which originated with Rosen [6]. In recent versions of the model, catastrophic failure is preceded by the growth of small clusters of fibre breaks wherein very short fibre segments see ever increasing loads until the failure of these adjacent fibres is virtually certain. The effective lengths over which these fibre segments are overloaded (taking into account statistical considerations of flaw density) are typically from 10 to 150 fibre diameters depending on such factors as the ratio of the fibre Young's modulus to the matrix shear modulus, the degree of plastic deformation and debonding near a break, and the variability in fibre strength. Because many commercial fibres have diameters of 4 to 15 μm, the failure models thus require knowledge of the strength distribution for fibres at a length scale from 0.05 to 1 mm. (See Phoenix *et al.* [9] for discussion on these points.)

The usual method for determining the distribution for fibre strength is by simple tension tests following standard techniques (ASTM D3379). Whereas a 20 mm gauge length is common, replications are often done at more than one gauge length to enhance extrapolation of the strength to shorter gauge lengths. But, because of technical difficulties with alignment, clamping and the tedium of manual testing, the gauge length is rarely less than 10 mm. Thus to determine the distribution for strength at much shorter length scales, as required by the above failure model, some version of Weibull/weakest-link scaling must be used.

In the simplest extrapolation, the Weibull scale parameter for strength, s_δ, at the length, δ, required by the model is approximately

$$s_\delta = s_L(L/\delta)^{1/\rho} \quad (1)$$

where L is the gauge length from the standard tension tests, and ρ is the Weibull shape parameter for fibre strength. For example, given a standard tensile test gauge length, L, of 20 mm, a characteristic load transfer length, δ, of 0.5 mm, and a Weibull shape parameter, ρ, of 5, yields $s_\delta = 2.1(s_L)$ which states that the strength at the length scale of the model is more than twice that measured in the tension tests. While

* *Present address*: Applied Remote Technology, Inc, 9950 Scripps Lake Drive, Suite 106, San Diego, CA 92131, USA.

0022–2461/91 $03.00 + .12

strengths of this magnitude have been observed from sophisticated microbending or loop tests, an extrapolation of this magnitude constitutes a large leap of faith and may be very inaccurate. This weakness compromises the predictive capability of the above models.

In the single-fibre composite test, a single fibre is embedded in a matrix such as epoxy to form a small dog-bone shape, and the dog-bone is increasingly strained to produce repeated fragmentation of the fibre. At some limiting strain, fragmentation ceases resulting in a distribution of short fibre lengths. Usually this final distribution is used with fibre strength statistics, extrapolated from tension tests, to determine the interfacial shear strength between the fibre and matrix. (See Netravali *et al.* [11] for examples and further references.) In this paper the emphasis is shifted from the estimation of the fibre interface strength to the estimation of the fibre strength statistics at gauge lengths comparable to the load transfer lengths around broken fibres in an actual composite. The experimental data, the number of breaks versus strain, can be gathered easily especially using acoustic emission [12], but the analysis requires an independent estimate of the average interfacial shear strength of the fibre/matrix system.

In this paper, we develop analytical approximations to the number of breaks as a function of strain for a single fibre in a composite tape. These approximations are easy to use and compare very favourably to results from a Monte Carlo simulation of the full problem by Henstenburg and Phoenix [13]. Rather than work with a single-filament composite, we work with a three-fibre composite, referred to as a "microcomposite", wherein a single graphite fibre is flanked on each side by a much larger glass fibre which has been proof-tested to strain that is roughly twice the strain to failure of the graphite fibre. This arrangement leads not only to better control of the applied strain at all points along the specimen, but also produces stress profiles in the fibres and matrix around fibre breaks more indicative of that which occurs in a large composite. The details of these stress profiles are investigated in a separate paper [14], and results from that study will be used in this analysis. We begin with a discussion of the fabrication of the three-fibre microcomposite tape.

2. Specimen fabrication

2.1. Materials

The three-fibre microcomposites were composed of IM-6 graphite fibres, (Hercules Corporation), SK glass fibres (Owens Corning Fiberglas), and DER 331/DEH 26 epoxy system (Dow Chemical Corporation). The graphite fibres were surface treated, but not coated with a surface finish, and were extracted from a 12 000 filament tow. Their nominal strain to failure at a gauge length of 20 mm is in the range of 1% to 2%, and they have an average modulus of elasticity of 280 GPa. The SK glass fibres were coated with an epoxy-compatible proprietary sizing, P365A, and were extracted from a 204 filament strand. These fibres have a larger nominal strain to failure of 3% to 5%, and an average elastic modulus of 90 GPa. The epoxy resin was diglycidyl ether of bisphenol A (DGEBA) with a resin molecular weight of 374. The hardening agent was tetraethylene pentamine (TEPA), an aliphatic polyamine. ASTM standard epoxy "dog-bone" specimens were fabricated from which an initial modulus of 2.80 GPa was determined, which is in agreement with values obtained on similar epoxies.

2.2. Microcomposite fabrication

The formidability of fabricating the microcomposite tapes can be appreciated by first reviewing their physical size. The target dimensions of the three-fibre microcomposite were 40 mm long (20 mm gauge length), 200 μm wide, and 50 μm thick. The graphite and glass fibres were 5.5 and 13 μm diameter, respectively. The interfibre spacing was to be held at 3 μm with a deviation of less than 1 μm over the sample length. Consequently, the fabrication of the samples required special techniques using micropositioners and optical microscopes.

The procedure for the fabrication of the microcomposites was broken down into a few basic tasks. The fibres were extracted from their yarns, aligned in the desired tape configuration, and embedded in an epoxy film. Then the undesired edge sections of the sample were removed and the resulting three-fibre microcomposite tape was tabbed for testing in a load frame. The load frame was built specifically to test microcomposites while under microscopic observation. The following sections will briefly describe the equipment designed and built to accomplish these tasks. Further details are given in Gulino [15].

2.2.1. Extraction

Three types of fibres were used in building the microcomposite samples. They were IM-6 graphite fibres, and SK and ET glass fibres. As mentioned, the IM-6 and SK fibres constituted the actual sample, while the ET fibres, with a diameter of about 30 μm, were used in creating the epoxy film surrounding the fibres of interest. After curing, the ET fibres were removed to obtain the desired microcomposite tape.

To obtain single graphite fibres, a 40 cm section of graphite tow was removed from the spool and placed in a basin filled with water. The graphite fibres were carefully separated, and 80 single fibres were extracted by pulling one end out of the basin on to a Teflon sheet. A 30 cm segment of each fibre was removed and stored, and the remaining segment was used to determine the cross-sectional area of the fibre using a specially built vibroscope [16]. The fibres used in the microcomposite tapes were randomly selected from this group of 80, and the remainder were tension tested to obtain Weibull strength statistics.

All the single glass fibres were extracted from 50 cm segments of strand, and their cross-sectional areas were determined. The fibres were separated from the strand by repeatedly peeling apart bundles until only a single fibre remained. The fibres were supported by a

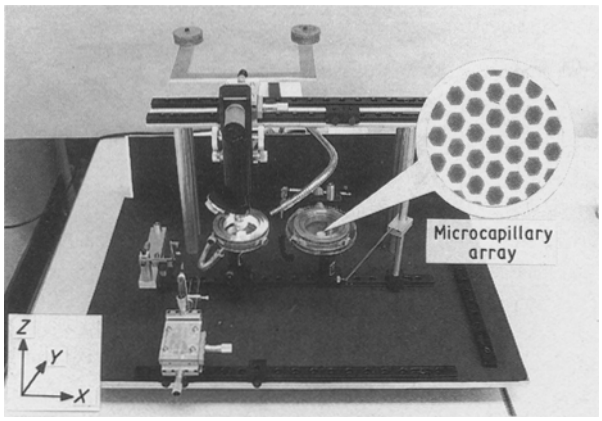

Figure 1 Apparatus for aligning the fibres.

board covered with black velvet cloth so that the fibres could be seen easily and would not be damaged during separation. The fibres were proof-tested at a 28.7 cm gauge length. For the SK fibres, the proof load was set so that the nominal strain in the fibres would be 3% (0.36 N), which would ensure that a graphite fibre would break repeatedly before the two glass fibres in the microcomposite tape broke. The stiffness for each surviving fibre was determined from the graph of load against displacement. These SK fibres were ordered by stiffness, and adjacent pairs were selected for use in the microcomposites. For the ET glass fibres, the proof load was 0.39 N, which was found to be adequate to ensure that the fibres would not break during specimen fabrication.

2.2.2. Alignment

Special equipment was built to manipulate and align the fibres prior to fabricating the microcomposite tape. The equipment consisted of a mechanical system of parallel optic rails, XY and XYZ micropositioners, a microscope, and microcapillary arrays on rotational stages, as shown in Fig. 1. The microcapillary arrays were 0.5 mm thick glass discs with 50 μm holes arranged in a hexagonal array with an approximately 50% volume fraction of holes (Fig. 1). The microcapillary arrays held the ends of the fibres creating a parallel arrangement of fibres, while the micropositioners were used to adjust their positions within the arrangement. To view the fabrication process, an optical microscope was mounted on an XY micropositioner above the fibres.

With the aid of the XYZ micropositioner, the ends of five glass fibres were threaded vertically through the two arrays. Two ET glass fibres were located at the edges, and the three centre fibres were SK glass fibres of which the outer two were destined for the microcomposite. The centre SK glass fibre was used to pull a graphite fibre, glued to one end, through the arrays to become its replacement (Fig. 2). The microcapillary arrays were then rotated from the horizontal plane to the vertical plane such that the fibres formed an essentially parallel arrangement.

Next, one set of fibre ends were fixed in a clamp and the opposite ends were glued to a cotton thread. The cotton threads were fed over rollers where a known tensioning weight was added. This procedure pretensioned every fibre while subjecting the fibre to minimal curvature. Next a small, but rigid, dipping frame was raised parallel to the fibres using a very stiff XZ micropositioner (Fig. 3). The spacing between the resulting planar array of fibres was determined by the projection of the fibre positions on to the dipping frame surface, which had been polished using standard metallographic techniques (Fig. 4). To vary the resulting spacing between the fibres, the arrays were rotated around an axis parallel to the length of the fibres, such that the resulting spacing on the surface of the dipping frame was greatly decreased with respect to the spacing determined by the holes in the microcapillary array. The rotational micropositioners could be positioned to within 1 arc minute which permitted small adjustments in the spacing between fibres. The space between the graphite and each SK glass fibre was about 3 μm and with less than a 1 μm deviation over the full length of the sample. This requirement often necessitated many iterations of rotating the microcapillary arrays, raising the dipping frame and observing the resultant fibre spacing. Once the desired spacing was obtained, the fibres were attached to the dipping frame by placing a drop of quick-setting epoxy on each end of the dipping frame.

2.2.3. Dipping

The role of the two, highly tensioned, ET glass fibres was to suppress surface tension effects on the three central fibres during the dipping process, as shown in Fig. 5. In the absence of external forces, the liquid epoxy would surround the fibres forming a cylinder along their length. Due to the gravitational forces, the liquid within this cylinder was drawn downward along

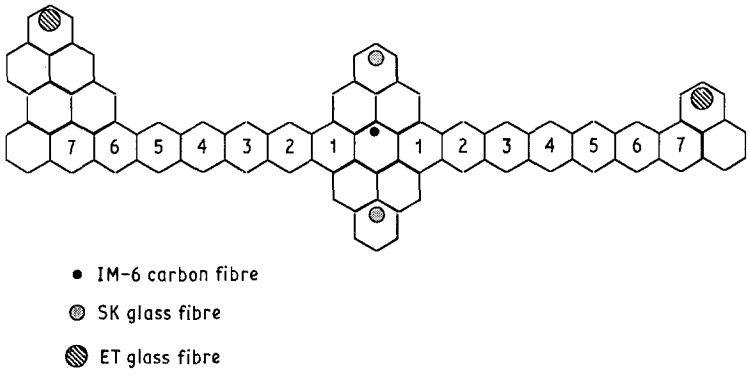

Figure 2 Schematic representation of the fibres positioned in the holes of the microcapillary array (non-essential holes deleted for clarity).

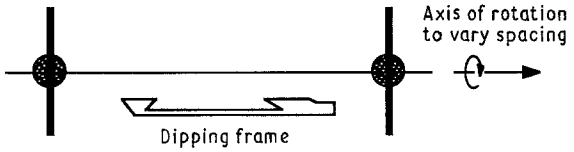

Figure 3 Side view of the dipping frame positioned beneath the aligned fibres.

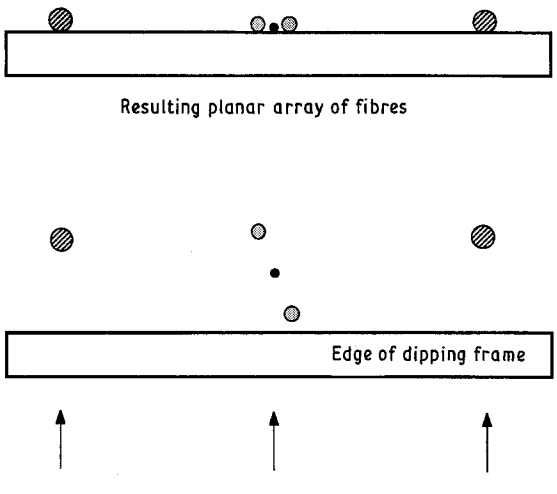

Figure 4 End view of the planar spacing obtained upon raising the dipping frame onto the fibres.

the fibres flattening the cylinder. The inward force due to the surface tension effects was reacted by the edge fibres which enabled the formation of a thin film. Without the edge fibres, the surface tension effects would destroy the spacing between the fibres achieved during alignment. In its design, the top edge of the dipping frame was undercut at an angle so that an epoxy film would be created only within the rectangular border between the two edge fibres and the frame ends. The edge fibres were placed approximately 900 μm from the three centre fibres.

The thickness and quality of the epoxy film depended strongly on the viscosity of the liquid epoxy, the speed at which the sample was dipped into and withdrawn from the liquid epoxy, and the spacing and tension in the edge fibres. The film thickness was reduced by decreasing the viscosity of the epoxy and the withdrawal speed, and by increasing the spacing between the ET edge fibres and the pre-tension in these fibres. These are not independent effects, and changing the value of one variable often imposed limits on the values of the others. For example, the viscosity was reduced by heating the epoxy. Yet the higher the temperature of the epoxy, the shorter the pot life which imposed a lower bound on the dipping and withdrawal speed. In addition, bubbles within the liquid increased the probability that a thin film would break during dipping, especially when the bubble diameter was of the order of the film thickness. Yet the more thoroughly the epoxy is degassed to

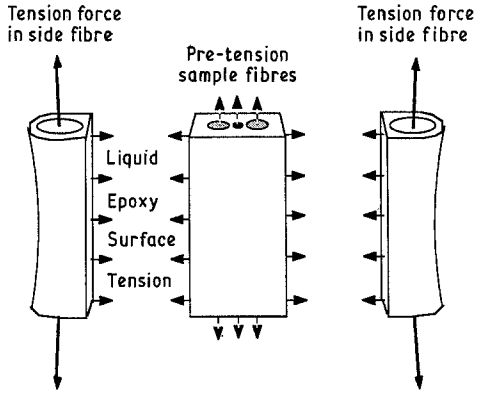

Figure 5 A free body diagram of the desired sample cut away from the edge fibres. The surface tension forces in the vertical direction are not shown.

remove the bubbles, the smaller the time left for dipping. Spacing the edge fibres further apart created a thinner film. Yet if the film was too thin, the film would often break during the epoxy curing cycle. The higher the tension in the edge fibres, the less they will be moved inward by the surface tension which resulted in an increased film thickness. Yet increasing the tension in the edge fibres increased the chance an edge fibre would break during the alignment process. Because a mathematical model of all these effects was too cumbersome, this process was optimized experimentally.

The following conditions were used in controlling the epoxy film thickness in the three-fibre microcomposite tapes. The edge fibres were pre-tensioned to 0.20 N, half of the proof load. The epoxy and curing agent were mixed at 40°C in stoichiometric proportions, degassed in a vacuum oven for 7 min and placed in a test tube. The dipping frame, which held the fibres in a planar array, was lowered into the test tube at 1.40 cm min^{-1} and subsequently withdrawn at 0.56 cm min^{-1} using a precisely controlled vertical slide. The dipping frame was subsequently placed horizontally on a Teflon sheet inside an oven, and the epoxy was cured at 80 °C for 3 h, after which the oven was turned off and allowed to cool slowly to room temperature.

2.2.4. Removing the edge sections

The edge sections, consisting of the ET glass fibres and part of the epoxy film, were removed by splitting the epoxy film symmetrically about the centre group of three fibres. This tedious process was accomplished using a specially designed apparatus consisting of two microscopes for viewing the sample, a set of closely spaced parallel razor blades, a rotational stage on to which the dipping frame was clamped, a Teflon-covered aluminium flat to support the specimen, and a system of micropositioners used to lower the blades through the epoxy film. Figs 6 and 7 show planar and cross-sectional views, respectively, of a specimen with removed edge sections.

2.2.5. Tabbing the microcomposites

The microcomposites were tabbed by sandwiching each end of the microcomposite tape between a square

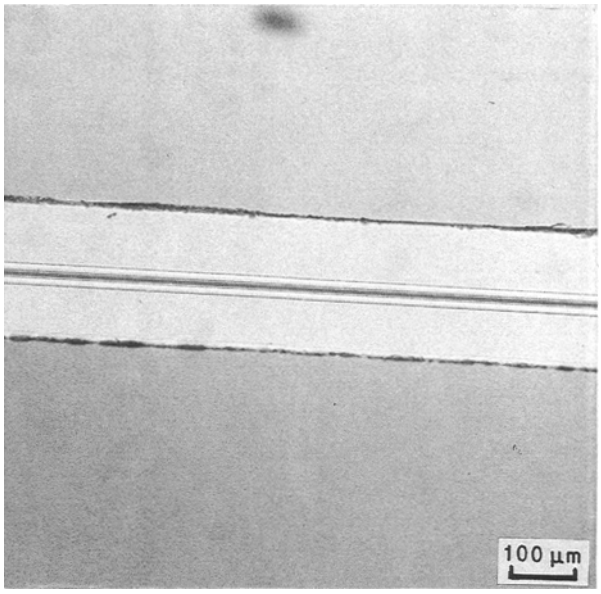

Figure 6 Top view of microcomposite sample after edge fibres have been removed.

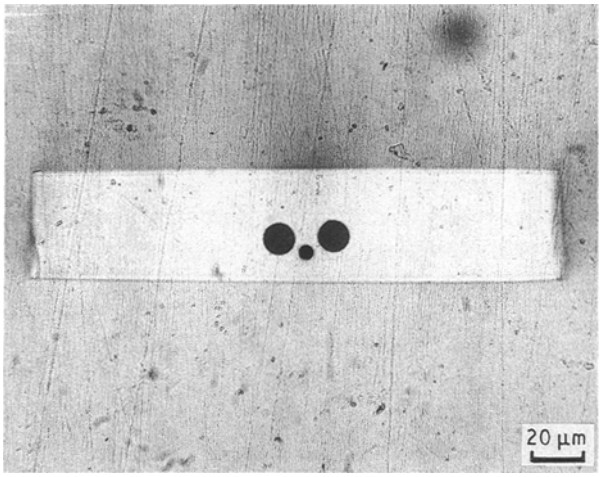

Figure 7 Cross-section of final microcomposite sample.

steel wafer, covered by a thin layer of adhesive, and a thin cardboard frame. The steel wafers minimized the deformation in the clamp region, and provided a hard flat region for clamping the sample on to the load frame. To ensure precise alignment of the microcomposite, a tabbing jig was used. The jig consisted of a Teflon-coated template to locate the microcomposite tape and the steel wafers, and a plexiglass slide which held the cardboard frame in position while the epoxy adhesive cured.

To tab the microcomposite tape, first the dipping frame, with the three-fibre microcomposite tape still attached, was fastened to the sample holder. By using the rotational stage and the *X YZ* micropositioner, the tape was aligned such that its vertical projection was aligned with the centre of the cardboard frame. This positioning was accomplished by viewing the sample through a microscope mounted directly above the template. The template surface had two centring lines scribed on it. These lines were 400 μm apart and were placed symmetrically about the centre line. The position for proper alignment was recorded and then the sample was moved away from the steel wafers. A thin layer of liquid epoxy was applied to the top surface of the steel wafers and to the opposing surfaces on the cardboard frame. The sample was returned to its previous position and lowered into the epoxy on the wafers. Next, the cardboard frame was pressed down sandwiching the sample against the steel wafers. The microscope objective was then lowered on to the top of the slide to apply moderate pressure to the assembly while the epoxy was curing. After the epoxy cured, the tabbed sample was removed for storage in a desiccator until testing.

3. Testing procedure

The testing of a three-fibre microcomposite tape was a detailed process in which the tape was held at a constant value of strain, and each break in the graphite fibre was observed through a plane polariscope enabling the load transfer to be visualized due to the photoelastic effects in the surrounding epoxy. The primary emphasis of the research effort was to characterize the load transfer around a single fibre, and due to the large number of breaks that could be studied in each sample and the difficulty in fabricating samples, two tapes, samples 11 and 12, were fully tested. Over 50 breaks had been observed when sample 11 broke at 3.46% strain, and 29 breaks had been observed in sample 12 at 3.10% strain when sample 12 was devoted to a brief study of viscoelastic effects in the epoxy. Sufficient information was obtained in the testing for the purposes of this study.

3.1. The load frame

The load frame was built specifically to apply a uniform strain to the microcomposite tape such that each break could be located and observed through a microscope. To accomplish this task a low-profile load frame was constructed which mounted on the stage of an inverted metallographic microscope. The load frame consisted of two moveable clamps that were constrained to translate in one direction by a set of linear ball bearings that rode on two parallel hardened steel shafts. One clamp was fixed to a load cell, which had a resolution of 0.01 N, and attached such that when the sample was clamped into the load frame the microcomposite axis was coincident with the axis of the load cell. The other clamp was driven by a non-rotating spindle micrometer. The end of the micrometer was attached to a motor with a stainless steel bellows coupling as shown in Fig. 8. The motor could translate with the microscope translational stage or just the motion of the micrometer. A special fixture was made that enabled a sheet polarizer to be placed between the sample and the microscope objective. The addition of the sheet polarizer allowed the sample to be viewed through a plane polariscope. The microscope was equipped with photographic attachments to record the photoelastic patterns. A dial gauge, held against the microscope stage, was used to determine the location of the fibre breaks along the specimen axis.

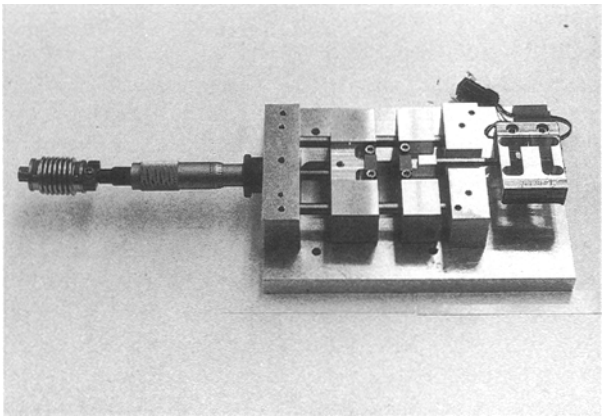

Figure 8 The load frame.

The load cell and the motor were independently calibrated. The complete load frame was checked for accuracy by measuring the stiffness of a light spring using both the load frame and an Instron 1130 tensile testing machine. The results were within 0.6%. The stiffness of a pre-tested glass fibre was measured to determine if considerable deformation was occurring within the clamp regions. Results for the modulus as compared to those from the Instron were within 1%.

In actual testing, a microcomposite tape was clamped into a load frame, and then loaded at a constant elongation rate to specific load level. The nominal load levels were determined by obtaining the initial modulus of the samples and then computing the loads corresponding to 0.1% increments of strain. At each load level, the number of breaks and their position in the sample were recorded. At selected breaks, measurements were made which characterized the load transfer. Because the matrix was undergoing mild load relaxation while the measurements were being made, the sample was allowed to recover at no load for at least twice the amount of time that it was under load.

3.2. Measurement of applied strain

A crucial aspect was to be able to determine accurately the strain in a specimen. Because epoxy contracts during curing and cooling, we first calculated the residual strain based on a straightforward mechanical model of the set-up (including the aluminium dipping frame and any pretensioning) and the elastic and thermal properties of the materials [15]. This residual strain in the graphite fibres was found to be about 0.05%, which is insignificant.

The applied tensile strain was determined by three different methods: in the first method, which was the most accurate, the strain was computed by using the relative displacements of the ends of the sample. The finite stiffness of the load cell was accounted for in this calculation, but any deformation in the tabs was neglected. The strain was also calculated by monitoring the positions of breaks with increasing load, an admittedly cruder method, but with consistent results. The strain was also estimated by using the initial modulus of the sample. This method proved accurate at low loads but, as expected, produced deviations as the matrix stress–strain rule became nonlinear.

After testing, each specimen was sectioned at equally spaced positions along the length of the specimen to measure the cross-sectional area of matrix, and thus, to uncover the possibility of any unevenness in strain along a specimen. In sample 11, the deviation from the average strain was estimated to be less than 5% of the average strain anywhere along the specimen. In sample 12, the observed deviation was within 3% over three-quarters of the specimen, but the deviation was 10% at one end of the specimen. The numbers of breaks in these regions were affected by this deviation but because the average strain was used, and because these regions were only a small part of the entire length of the specimen, their effect on the analysis is negligible. For example, a 10% deviation in 20% of the specimen length for a Weibull shape parameter of 5 produces only a 2% deviation in the total expected number of breaks.

3.3. Tension tests on the graphite fibres

Out of the eighty fibres, 65 were not used in microcomposite tape fabrication. Of these, 58 were tension tested in an Instron 1130 tensile tester at a 20 mm gauge length and $0.0254\,\text{min}^{-1}$ strain rate, using standard tabbing techniques. The remaining 7 were tension tested at an 8 in. gauge length to confirm the fibre elastic modulus.

4. Analysis for fibre break progression

The break progression of the graphite fibre in the strained microcomposite tape was modelled by assuming the flaws were distributed along the fibre according to a homogeneous, compound Poisson process. The average number of flaws per unit length with strength less than or equal to a given stress, s, was assumed to follow a power law in stress. Thus the resulting distribution for the strength of a single fibre in simple tension has the familiar Weibull form, as seen shortly.

When a fibre breaks, the fibre retracts locally, producing a shear force in the matrix; but at some distance from the break the fibre maintains the previous level of stress. In reality, this load recovery length and the associated shear profile depend on a variety of factors such as the longitudinal stiffness of the fibres, the shear stiffness of the matrix, the plastic yield strength and limiting plastic shear strain of the matrix, and the local volume fraction of fibres. A full analysis of the specimens in this study will be presented elsewhere [14]. Here, it suffices to proceed with a simplified version, in order to make the probability analysis tractable.

As the applied stress is increased, the fibre breaks repeatedly until the fragment lengths are too small to achieve further increases in stress within the middle portion of some fragment. At this point the break progression ceases. Thus the fragmentation process can be equivalently thought of as the initiation and growth of load recovery regions activated by stress sensitive flaws. In the following paragraphs, the number of breaks as a function of applied stress will be

modelled using this concept. Two assumptions will be made to simplify the problem: first, the shear stress in the load recovery region will be considered constant (as though the matrix were perfectly plastic, where the plastic flow stress can be interpreted as the average shear stress in the load recovery region). Second, the interaction of adjacent load recovery regions will be ignored. The second assumption is reasonable at moderate stresses, but as the stress approaches the fragmentation limit, and a large fraction of the fibre length is covered by load recovery regions, such interactions will be significant.

The expected number of breaks as a function of the applied strain will be obtained using two different approaches. First, the problem will be solved by conditioning on the number of observed breaks, whereas in the second approach the problem will be solved by conditioning on the total number of flaws at a specific stress level. Using the first approach, an explicit approximation is developed for the mean number of breaks in a specimen as a function of stress level. Using the second approach, a numerical scheme is developed for computing both the mean number of breaks at a fixed stress and confidence intervals about the mean. It will be possible to assess the importance of neglecting interactions between adjacent load recovery regions in the derivation by comparing the present approximations with results from a Monte Carlo simulation developed by Henstenburg and Phoenix [13].

4.1. Approximate probabilistic model for break progression

According to the Poisson model, the probability of n flaws occurring with strength less than or equal to stress, s, and in length, L, is

$$P[N(s, L) = n] = \frac{[\mu(s, L)]^n}{n!} e^{-\mu(s, L)} \quad s \geqslant 0, L \geqslant 0 \tag{2}$$

where $\mu(s, L)$ is the mean number of flaws with strength less than or equal to s, within length L, and n is a non-negative integer.

The mean of this Poisson distribution, $\mu(s, L)$, is assumed to follow a power law in stress such that the fibre strength distribution is a two-parameter Weibull distribution. That is we take

$$\mu(s, L) = \lambda(s)L \tag{3}$$

where

$$\lambda(s) = (1/L_0)(s/s_0)^\rho \tag{4}$$

is the mean number of flaws per unit length with strength less than or equal to s, and where ρ, s_0 and L_0 are positive constants.

The parameter ρ becomes the Weibull shape parameter and s_0 the Weibull scale parameter, respectively, for the strength of fibres of length L_0. This follows from the fact that the probability of one or more flaws existing in length L, with strength less than or equal to s, is

$$P[N(s, L) \geqslant 1] = 1 - P[N(s, L) = 0] = 1 - e^{-(L/L_0)(s/s_0)^\rho} \tag{5}$$

where the last expression is the desired Weibull distribution when L is taken as L_0. Indeed this result allows us to scale to an arbitrary length L, as is well known.

4.1.1. Approach I: conditioning on the number of breaks

To model the progression of the number of breaks with stress, the flaws with strength less than or equal to s are divided into two categories; flaws which cause breaks, and flaws which lie within the load recovery regions of breaks and are thus obscured. The situation is depicted in Fig. 9. This representation can be quantified by introducing the following random variables:

$N_t(s, L)$ = the total number of flaws in length, L, and with strength less than or equal to s.

$N_b(s, L)$ = the number of breaks in length, L, and at stress less than or equal to s.

$N_0(s, b)$ = the number of flaws obscured within the load recovery region around a fibre break at stress less than or equal to s, where b denotes the length of the load recovery region.

The relationship between these variables is expressed by the equality

$$N_b = N_t - \sum_{j=1}^{N_b} N_0, j \tag{6}$$

where j is the jth observed break. By taking expectations, the mean number of breaks is determined as

$$E(N_b) = E(N_t) - E\left(\sum_{j=1}^{N_b} N_0, j\right) \tag{7}$$

where $E(N_t)$ is the expected value of the Poisson random variable, N_t, and is equal to $\mu(s, L)$.

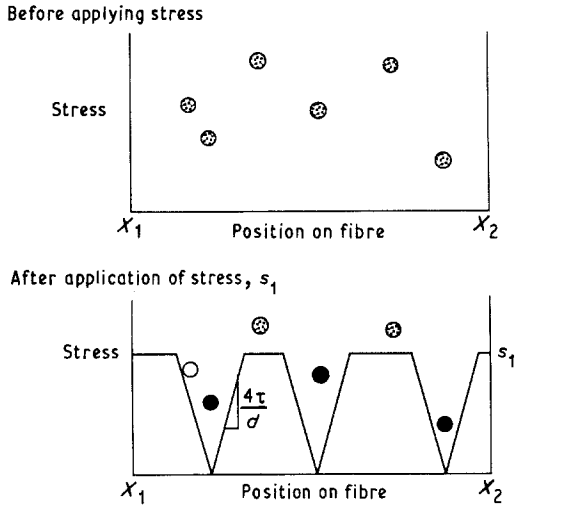

Figure 9 Two-dimensional representation of flaws within a single fibre before and after application of the stress, s_1.

To complete this derivation the expectation of the sum of the number of flaws obscured must be approximated. This task may be accomplished by relating the number of flaws obscured to the number of flaws in a load recovery region (lrr), that is the region in stress and position bounded by the applied stress, s, and the stress profile around a break. The mean number of flaws within such a region, $\mu(\text{lrr})$, is determined by integrating the flaw density (derivative of Equation 4) over this region. Because the flaws are distributed according to a compound Poisson process, and therefore a process with independent stationary increments along the fibre, the calculation of the mean number of flaws within the load recovery region does not depend on its longitudinal location. Thus we have

$$\begin{aligned}\mu(\text{lrr}) &= 2\int_0^{sd/4\tau}\int_{4\tau x/d}^{s} {}^{1}/L_0(s'/s_0)^{\rho-1}(\rho/s_0)\,ds'\,dx \\ &= \left(\frac{\rho}{\rho+1}\right)(sd/2\tau)\frac{1}{L_0}(s/s_0)^{\rho} \\ &= \left(\frac{\rho}{\rho+1}\right)\beta\lambda \end{aligned} \tag{8}$$

where

$$\beta = (sd/2\tau) \tag{9}$$

is the load recovery length, τ is the shear stress on the fibre surface, and d is the fibre diameter.

The number of flaws within a given load recovery region, N_{lrr}, follows a Poisson distribution with mean, $\mu(\text{lrr})$. The probability that k flaws are within the load recovery region is

$$P(N_{\text{lrr}} = k) = \frac{[\mu(\text{lrr})]^k}{k!}e^{-\mu(\text{lrr})} \tag{10}$$

The expected value of the total number of obscured flaws may be calculated by conditioning on the number of observed flaws along the fibre. Thus the expectation can be expessed as

$$\begin{aligned}\mathrm{E}\left(\sum_{j=1}^{N_b} N_0\right) &= \sum_{k=1}^{\infty}\mathrm{E}\left[\left(\sum_{j=1}^{k} N_0\right)\middle| N_b = k\right] \\ &\quad P(N_b = k)\end{aligned} \tag{11}$$

The expectation within the sum can be simplified by using the independence of disjoint areas, neglecting interactions between adjacent load recovery regions, and then using an equivalent representation for the number of obscured flaws in terms of the Poisson random variable, N_{lrr}. We have

$$\begin{aligned}\mathrm{E}\left[\left(\sum_{j=1}^{k} N_0\right)\middle| N_b = k\right] &= k\mathrm{E}(N_0|N_b = 1) \\ &= k\sum_{m=1}^{\infty} mP(N_{\text{lrr}} = m+1|N_{\text{lrr}} \geqslant 1)\end{aligned} \tag{12}$$

which reflects the fact that one of the flaws in the load recovery region is actually the cause of the break, and thus, cannot be counted as obscured. Upon substitution of Equation 12 into Equation 11, we obtain

$$\begin{aligned}\mathrm{E}\left(\sum_{j=1}^{N_b} N_0\right) &= \sum_{k=1}^{\infty} kP(N_b = k) \\ &\quad \times \sum_{m=1}^{\infty} mP(N_{\text{lrr}} = m+1|N_{\text{lrr}} \geqslant 1) \\ &= \mathrm{E}(N_b)\sum_{m=1}^{\infty} mP(N_{\text{lrr}} = m+1|N_{\text{lrr}} \geqslant 1)\end{aligned} \tag{13}$$

Upon evaluating the infinite sum in Equation 13 (which requires calculating a conditional probability using Equation 10), we obtain

$$\mathrm{E}\left(\sum_{j=1}^{N_b} N_0\right) = \mathrm{E}(N_b)\left(\frac{\mu(\text{lrr})}{1-e^{-\mu(\text{lrr})}} - 1\right) \tag{14}$$

Upon substituting Equation 14 into Equation 7, we obtain an estimate of the mean number of breaks as

$$\mathrm{E}(N_b) = \mu(s, L)\left(\frac{1-e^{-\mu(\text{lrr})}}{\mu(\text{lrr})}\right) \tag{15}$$

This equation can be nondimensionalized directly by first nondimensionalizing the expression in the exponent. We write

$$\begin{aligned}\mu(\text{lrr}) &= \left(\frac{\rho}{\rho+1}\right)(sd/2\tau)\frac{1}{L_0}(s/s_0)^{\rho} \\ &= \left(\frac{\rho}{\rho+1}\right)\left(\frac{s}{s^*}\right)^{\rho+1}\end{aligned} \tag{16}$$

where

$$s^* = \left(\frac{2\tau L_0}{ds_0}\right)^{1/(\rho+1)} s_0 \tag{17}$$

The only term left to nondimensionalize is $\mu(s, L)$. We write

$$\mu(s, L) = \frac{L}{L_0}\left(\frac{s}{s_0}\right)^{\rho} = \left(\frac{L}{b^*}\right)\left(\frac{s}{s^*}\right)^{\rho} \tag{18}$$

where

$$b^* = \left(\frac{2\tau L_0}{ds_0}\right)^{-\rho/(\rho+1)} L_0 \tag{19}$$

is a normalizing length. Dividing s^* by b^* yields the simple relation

$$\frac{s^*}{b^*} = \frac{2\tau}{d} \tag{20}$$

which has the interpretation that when the stress equals s^*, the load recovery length is b^*. The load recovery length consists of the length for load recovery from both ends of the broken fibre. Note that the nondimensionalization in Henstenburg and Phoenix [13] is equivalent to the nondimensionalization developed here, except that the dimensionless length, h^*, there is half the quantity, b^*, here.

The mean number of breaks in terms of the nondimensional parameters is

$$\begin{aligned}\mathrm{E}(N_b) &= \left(\frac{L}{b^*}\right)\left(\frac{\rho+1}{\rho}\right)\left(\frac{s^*}{s}\right) \\ &\quad \times \{1 - \exp[-\rho/(\rho+1)](s/s^*)^{\rho+1}\}\end{aligned} \tag{21}$$

Normalizing the expected number of breaks by L/b^*, yields the break density, denoted Δ, and normalizing the stress s, by s^*, yields the nondimensional stress, denoted σ. Thus, in terms of the nondimensional variables, Equation 21 becomes

$$\Delta = \left(\frac{\rho + 1}{\rho}\right)\sigma^{-1}(1 - \exp[-[\rho/(\rho + 1)]\sigma^{\rho+1}]) \quad (22)$$

4.1.2. Approach II: conditioning on the total number of flaws at a fixed stress level

The break progression can be described in greater detail by computing the probability of all possible outcomes at a fixed stress level, s. By conditioning on the total number of flaws with strength less than s, each flaw can be placed according to one of two possible outcomes: the flaw can either be observed as a break or obscured by the load recovery region of an existing break. For each possible number of total flaws, n, there are at most n breaks. The outcome of i breaks given j flaws will be represented by $S_{i,j}$, $0 \leqslant i \leqslant j, 0 \leqslant j$, which may be thought of as the states of a Markov chain [17]. In order to calculate the probability for each state, we must first determine transition probabilities from state to state. In this analysis, the flaws are viewed as being placed sequentially. The first flaw will always move the process to the state, $S_{1,1}$, because a break is certain. The next flaw causes the process to move either to $S_{1,2}$ or to $S_{2,2}$. Generally if the flaw falls within the stress-position space that is not in a load recovery region, the flaw will register as a break. If it does not cause a break, it must have fallen within the load recovery region of another flaw. Thus, the addition of a flaw increases the number of observed breaks by either one or zero, and the placement of each flaw can be viewed as a transition of a random process between states. The transition probability of moving from $S_{i,j}$ to $S_{i,j+1}$ is defined as T_i, and therefore the transition probability of moving from $S_{i,j}$ to $S_{i+1,j+1}$ must be $(1 - T_i)$. The set of all possible states and the transitions between states can be represented by a triangular grid as shown in Fig. 10.

Conditioned on a fixed number of flaws, $N_t = j$, the probability of a flaw falling within a subset, A, of the entire permissible region is [17]

$$P[\text{Flaw lies within region A} \mid N_t = j] = \frac{\mu(A)}{\mu(s, L)} \quad (23)$$

Thus because overlap between adjacent load recovery regions is ignored, we have

$$T_i = \frac{i\mu(\text{lrr})}{\mu(s, L)} \quad (24)$$

By using the transition probabilities, the probability for each progressive state may be found from

$$P_{i,j} = T_i P_{i,j-1} + (1 - T_{i-1})P_{i-1,j-1} \quad (25)$$

for $i \leqslant j \leqslant N_t$, where $P_{i,j}$ is the probability of being in state $S_{i,j}$. The probability of observing i breaks, P_i, is

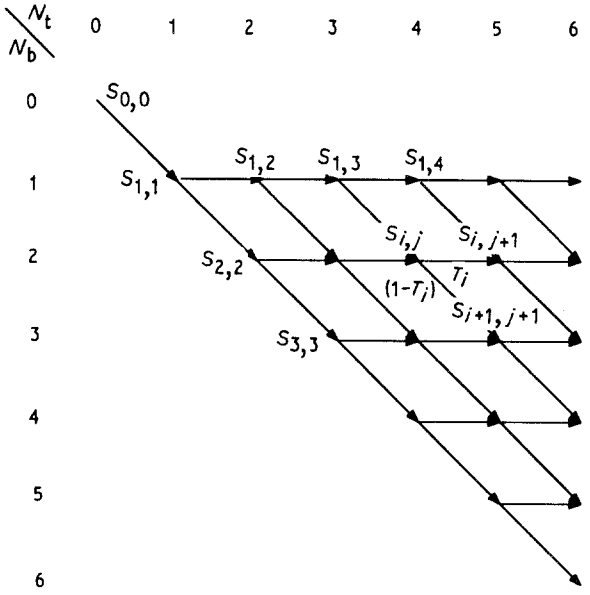

Figure 10 Grid representation of all possible states, $S_{i,j}$, and all possible transitions between the states.

thus

$$\sum_{j=i}^{\infty} P_{i,j} P(N_t = j) \quad (26)$$

Because $P(N_t = j)$ is a probability mass function with finite moments, the series can be truncated without significantly affecting the probability calculation for subsequent states. The process was terminated for a given i, at a value of j where the probability of j flaws occurring was less than 10^{-10}, and j was greater than the expected number of flaws at the particular value of the applied stress. The latter constraint was imposed so that the process would not be terminated prematurely. Also, the process was truncated at state i when the probability of being in state i was less than 10^{-10}, where again i had to be greater than the expected number of flaws.

Once the probabilities for each state were known, symmetric confidence intervals (K', K''), with confidence coefficient $1 - \alpha$, were determined. The lower limit, K', on the confidence interval was found by determining the largest integer k such that $P_k \leqslant \alpha/2$. The upper limit, K'', was found by determining the smallest k such that $P_k \geqslant 1 - \alpha/2$. The mean number of breaks, $E(N_b)$, was computed by definition,

$$E(N_b) = \sum_{i=1}^{i_{max}} iP_i \quad (27)$$

where the applied stress, s, is implicit.

4.2. Comparison of the mean number of breaks with results from Monte Carlo simulation

To check the accuracy of these approximations, the variation break density, Δ, with the nondimensional stress, σ, was compared to results obtained by a Monte Carlo simulation of the full problem using the software of Henstenburg and Phoenix [13]. In the simulation, the overload regions were allowed to interact. The approximate method displayed close

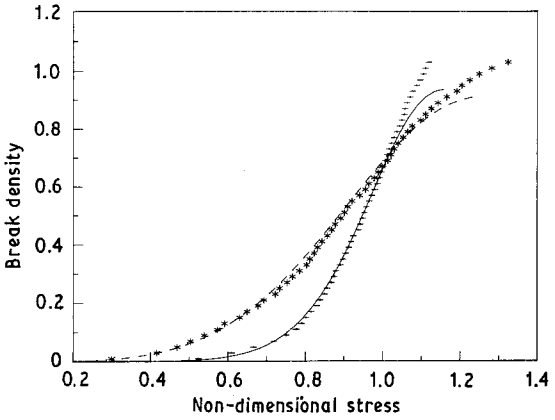

Figure 11 Comparison of the approximate model (——ρ = 8, – – – ρ = 4) for break progression with the average of five runs of a simulation [13] (+ ρ = 8, *ρ = 4).

agreement with the simulation up to a nondimensional stress value of one, as shown in Fig. 11. The expected fraction of the gauge length, as a function of the nondimensional stress, contained within the load recovery regions can be shown to be

$$\frac{E(N_b)\beta}{L} = \left(\frac{\rho + 1}{\rho}\right) \{1 - \exp[-(\rho/\rho + 1)(\sigma)^{\rho+1}]\} \quad (28)$$

When $\sigma = 1$, and $\rho = 6$, approximately two-thirds of the gauge length would be in the load recovery region, neglecting interaction between adjacent load recovery regions. An explanation for the approximate solution folding under the simulation results at high stresses is that when the stress equals s^* (that is, $\sigma = 1$) one flaw is expected in the load recovery length b^*. Thus, the largest stress which allows for an accurate approximation can be interpreted as the point where the expected number of flaws within the length of a single load recovery region equals one. The error in the approximate model arises from an overestimation of the number of obscured flaws. When the breaks are close together, the load recovery regions can overlap, and in the approximation, counts a flaw within the overlap twice.

5. Analysis of experimental break progression

First, the results of the tension tests on the single graphite fibres (20 mm gauge length), are shown in the form of a Weibull plot in Fig. 12. The respective Weibull shape and scale parameter values, $\rho = 5.6$ and $s_0 = 5010$ MPa, were estimated by the method of maximum likelihood. These results are consistent with those obtained by Phoenix *et al.* [9] on the same spool of IM-6 graphite fibre (though an interpolation suggests very slightly higher strength in the present case).

To apply the model to the break progression in the three-fibre composites, the actual load recovery regions were interpreted as zones which could not experience a higher stress with increased applied strain. By using the length of the debond plus plastic zone at 3.1% applied strain, as seen optically and by photoelastic techniques [14, 15], the average shear

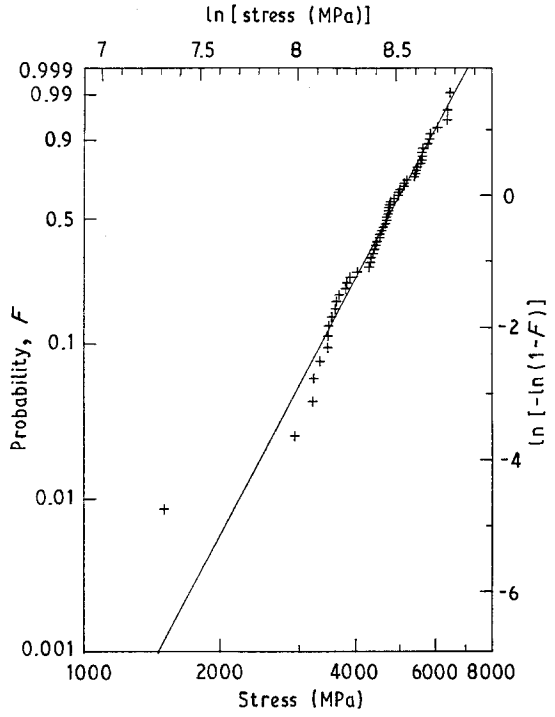

Figure 12 Weibull plot of tension tests results on single fibres. ρ = 5.6, s = 5010 MPa, L_0 = 20 mm.

stress on the fibre was computed to be 61 MPa. Using this average value of the shear stress for τ, and the Weibull shape and scale parameters estimated from the tension tests on the 20 mm gauge length fibres, the break progression in samples 11 and 12 was predicted using the formulae in the previous section. The results are shown in Fig. 13. The hypothesis that the break progression could be predicted using the Weibull strength parameters obtained at a standard gauge length of 20 mm, was rejected at the 99% significance level as indicated by the dotted lines.

Because the nondimensional parameters (see Equation 21), characterize the break progression, these parameters were estimated by a visual best fit to the data. The fit, shown in Fig. 14, was carried out such that the computed curve began to fold under the data as the nondimensional stress exceeded one. The estimated Weibull parameters and corresponding length, b^*, are given in Table I. At the same time, from the tension test data obtained at the gauge length of 20 mm, we also plotted the scale parameter value as a function of length, using the usual Weibull weakest link scaling. The results are shown in Fig. 15. Clearly the usual extrapolation of Equation 1 overestimated the strength of the fibres at the small, approximately 0.5 mm, gauge length characteristic of the scale of load transfer.

6. Discussion and conclusions

The hypothesis that the break progression of the graphite fibre in the three-fibre microcomposite tape could be predicted using the Weibull strength parameters obtained from tension tests on single fibres at a gauge length of 20 mm was rejected at the 99% significance level. This result depends, of course, on the accuracy of the strain measurements in each sample.

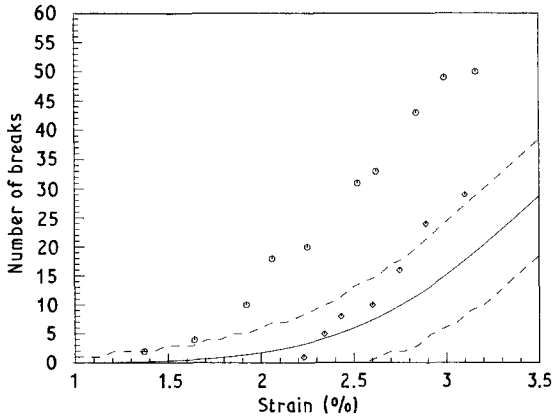

Figure 13 Experimental break progression data (——) compared with a 99% confidence band (– – –) around the mean number of breaks as predicted from the 20 mm tension results, from samples (Ⓞ) 11, and (◇) 12.

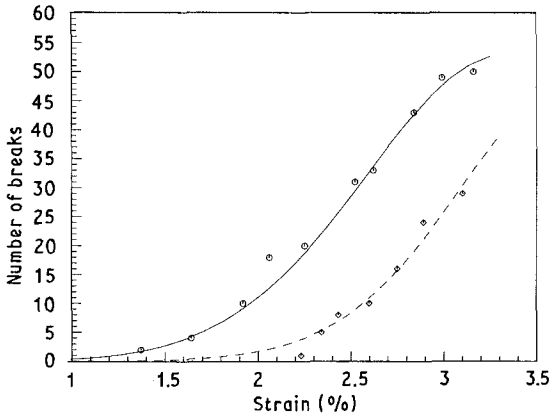

Figure 14 Estimation of Weibull parameters for fibre strength from break progression data using a best fit of Equation 21. (——) $s^* = 7.6$ GPa, $b^* = 0.34$ mm; (– – –) $s^* = 8.8$ GPa, $b^* = 0.40$ mm. (Ⓞ) Sample 11, (◇) sample 12.

TABLE I Estimated characteristic parameters for the break progression in samples 11 and 12

Sample	s^* (GPa)	b^* (mm)	ρ
11	7.6	0.34	5.0
12	8.8	0.44	7.8

The measurement of the applied strain was verified by the load transfer measurements made on samples 11 and 12 as reported elsewhere [14, 15]. These measurements showed no discrepancy between samples 11 and 12 as a function of strain even though the number of breaks observed in sample 11 was almost double the number observed in sample 12 at 3.1% strain.

Although the break progression for each sample could be fitted to the Poisson/Weibull model, the flaw density (derivative of Equation 4) appeared to differ for the two extracted fibres. This observation would appear to contradict the conclusion implicit in the tension test studies in Phoenix *et al.* [9], that the Poisson/Weibull model works for graphite fibres with one function $\lambda(s)$ for all fibres. It should be pointed out, however, that the bulk of the strengths observed in their study cover a much lower strain range than seen in the break progression here. For example

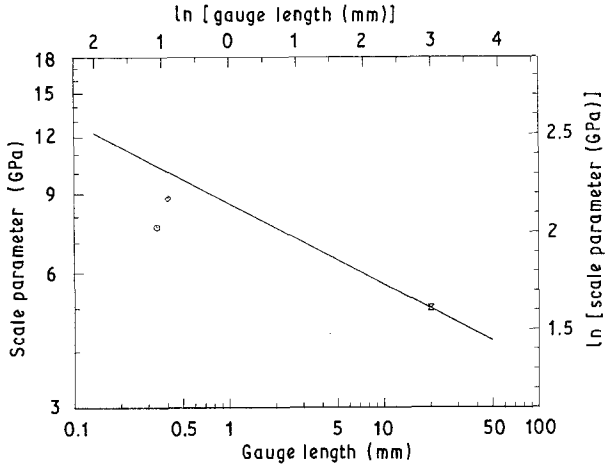

Figure 15 Log–log plot of the Weibull scale parameter for strength against gauge length, showing results from samples (Ⓞ) 11 and (◇) 12 compared to the Weibull weakest link extrapolation (——) of the tension test data (⧖) at 20 mm.

5.5 GPa corresponds to 2% strain, which is in the lower tail of Figs 13 and 14. Thus it is possible for the homogeneous Poisson model of Equation 4 to apply at low stresses but not at higher stresses where different, nonhomogeneous, flaw mechanisms for very high strength flaws may be operative from fibre to fibre, or at different positions along a fibre.

The number of breaks versus strain, predicted from the Weibull parameters estimated from the tension tests, fell below the experimental data. For sample 11, the scale parameter at the length scale of load transfer, was predicted to be 36% greater than actually determined using the experimental break progression. It is important to consider the influence of the value of τ on the predictions and experimental results. It can be seen from Equations 17 and 19 that the value of τ has only a mild effect on the dimensionless stress s^*, but the length b^* is almost inversely proportional to τ. Thus it can be seen that an experimentally different value of τ would, in principle, not affect the early break progression in Fig. 14, but would affect the upper termination point. Although, a very large error in τ is necessary, roughly a factor of 3 decrease, for the value of the estimated scale parameter, b^*, to agree with the Weibull weakest link estimate. Indeed there is some indication, from the distributions of Phoenix *et al.* [9] obtained at the highest stresses and shortest gauge lengths, that a "levelling off" of strength with decreasing length may be occurring (see Fig. 5 in [9]) which would agree with the results found here.

On average, both fibres had strengths significantly lower, roughly 25%, than predicted by this Weibull weakest link scaling (Equation 1). Thus, it is possible to perform "typical" tension tests (at say a 20 to 50 mm gauge length) on single fibres extracted from two different spools of the same lot, obtain the same Weibull parameters, and then erroneously conclude these two spools will yield composites with equivalent strength, because the fibre strengths at short gauge lengths (near 0.5 mm), which directly affect composite strength, may differ substantially.

These results also have an impact on the use and interpretation of the single-fibre composite technique.

The differences between fibres in the estimated Weibull parameters at short gauge lengths suggest the need to test many samples before estimating the interfacial shear strength. Moreover, the estimation of the interfacial shear strength using the single-fibre composite technique requires the fibre strength at short gauge lengths and therefore extrapolation of tension test results may lead to poor estimates of the interfacial shear strength. In addition, this study points out the weakness in using only the final fragment distribution in the computation of the interfacial shear stress, because there is more than one combination of b^*, s^*, and the interfacial shear stress which could produce the same average fragment length.

Acknowledgement

This work was supported by the Cornell University Materials Science Center, an NSF DMR-MRL.

References

1. S. B. BATDORF, *J. Reinf. Plastics Compos.* **1** (1982) 153.
2. S. B. BATDORF and R. GHAFFARIAN, *ibid.* **1** (1982) 165.
3. S. L. PHOENIX and R. L. SMITH, *Int. J. Solids Struct.* **19** (1983) 479.
4. R. L. SMITH, S. L. PHOENIX, M. R. GREENFIELD, R. B. HENSTENBURG and R. E. PITT, *Proc. R. Soc. Lond.* **388** (1983) 353.
5. A. S. WATSON and R. L. SMITH, *J. Mater. Sci.* **20** (1985) 3260.
6. B. W. ROSEN, *AIAA J.* **2** (1964) 1985.
7. R. D. JAMISON, *Compos. Sci. Technol.* **24** (1985) 83–99.
8. N. J. WADSWORTH and I. SPILLING, *Brit. J. Appl. Phys. Ser. 2*, **1** (1968) 1049.
9. S. L. PHOENIX, P. SCHWARTZ and H. H. ROBINSON IV, *Compos. Sci. Technol.* **32** (1988) 81.
10. J. M. LIFSHITZ and A. ROTEM, *J. Compos. Mater.* **6** (1972) 358.
11. A. N. NETRAVALI, R. B. HENSTENBURG, S. L. PHOENIX and P. SCHWARTZ, *Polym. Compos.* **10** (1989) 226.
12. A. N. NETRAVALI, L. T. T. TOPOLESKI, W. H. SACHSE and S. L. PHOENIX, *Compos. Sci. Technol.* **35** (1989) 13.
13. R. B. HENSTENBURG and S. L. PHOENIX, *Polym. Compos.* **10** (1989) 389.
14. R. GULINO and S. L. PHOENIX, *J. Mater. Sci.* in press.
15. R. GULINO, PhD thesis, Cornell University, Ithaca, New York (1988).
16. H. H. ROBINSON IV, H. F. WU, M. AMES and P. SCHWARTZ, *Rev. Sci. Instrum.* **58** (1987) 436.
17. H. M. TAYLOR and S. KARLIN, in "An Introduction to Stochastic Modelling" (Academic Press, New York, 1984).

Received 24 July
and accepted 22 November 1989